Parameterised diabatic processes in numerical simulations of an extratropical cyclone

Article

Published Version

Open Access

RMetS

Royal Meteorological Society

Parametrized diabatic processes in numerical simulations of an extratropical cyclone

O. Martínez-Alvarado* and R. S. Plant

Department of Meteorology, University of Reading, UK

*Correspondence to: O. Martínez-Alvarado, Department of Meteorology, Earley Gate, PO Box 243, Reading RG6 6BB, UK.
E-mail: o.martinezalvarado@reading.ac.uk

The parametrization of diabatic processes in numerical models is critical for the accuracy of weather forecasts and for climate projections. A novel approach to the evaluation of these processes in models is introduced in this contribution. The approach combines a suite of on-line tracer diagnostics with off-line trajectory calculations. Each tracer tracks accumulative changes in potential temperature associated with a particular parametrized diabatic process in the model. A comparison of tracers therefore allows the identification of the most active diabatic processes and their downstream impacts. The tracers are combined with trajectories computed using model-resolved winds, allowing the various diabatic contributions to be tracked back to their time and location of occurrence.

We have used this approach to investigate diabatic processes within a simulated extratropical cyclone. We focus on the warm conveyor belt, in which the dominant diabatic contributions come from large-scale latent heating and parametrized convection. By contrasting two simulations, one with standard convection parametrization settings and another with reduced parametrized convection, the effects of parametrized convection on the structure of the cyclone have been determined. Under reduced parametrized convection conditions, the large-scale latent heating is forced to release convective instability which would otherwise have been released by the convection parametrization. Although the spatial distribution of precipitation depends on the details of the split between parametrized convection and large-scale latent heating, the total precipitation amount associated with the cyclone remains largely unchanged. For reduced parametrized convection, a more rapid and stronger latent heating episode takes place as air ascends within the warm conveyor belt.

Key Words: extratropical cyclone; diabatic process; large-scale–convective precipitation split

Received 2 May 2013; Revised 9 August 2013; Accepted 3 September 2013; Published online in Wiley Online Library 2 December 2013

1. Introduction

Extratropical cyclones are responsible for much of the weather variability at midlatitudes, and are important for the planetary-scale energy budget by transporting energy from the Tropics polewards (e.g. Oort and Peixóto, 1983; Peixóto and Oort, 1984; Trenberth and Stepaniak, 2003; Messori and Czaja, 2013). Their practical importance is evidenced by the economic impact associated with the strong winds and heavy precipitation that these weather systems can produce. For instance, one single event, windstorm *Kyrill* on 18 January 2007, caused insured losses of up to $2.7 billion ($4.3 billion) and economic losses of at least twice as much (Pinto *et al.*, 2012).

The effects of diabatic processes within extratropical cyclones have been extensively investigated from theoretical (e.g. Montgomery and Farrell, 1991; Whitaker and Davis, 1994), observational (e.g. Tracton, 1973; Schäfler *et al.*, 2011) and modelling (e.g. Stoelinga, 1996; Didone, 2006) perspectives.

Latent heat release has often been considered to be an important factor in cyclogenesis (e.g. Sanders and Gyakum, 1980; Davis *et al.*, 1993; Zhu and Newell, 1994; Wernli *et al.*, 2002) and may even take a leading role in some cases, serving as a surrogate for a surface temperature gradient (e.g. Ahmadi-Givi *et al.*, 2004). However, its role is highly case-dependent, being sensitive to the horizontal heating configuration, for example (Smith, 1999).

Extratropical cyclones are relatively well forecast at the synoptic scale. However, the forecasting of embedded structures at smaller scales is more difficult. This is in part due to a lack of understanding of the interactions that take place between the various parametrized diabatic processes in the models, as well as the interactions between the parametrized processes and the large-scale atmospheric dynamics. Collectively such interactions determine the evolution and strength of simulated mesoscale structures. Various studies of diabatic processes in extratropical cyclones have begun to unravel some of the interactions with numerical models. For example, Stoelinga (1996) introduced a

decomposition of potential vorticity in terms of diabatic processes, and related approaches have been followed in subsequent studies (e.g. Chagnon *et al.*, 2013). Recently Joos and Wernli (2012) have devised a trajectory–based decomposition of microphysical processes in the warm conveyor belt in order to explain changes in potential vorticity within this stream. In contrast, another recent study (Fink *et al.*, 2012) has taken a different approach by inferring the proportion of the surface pressure tendency that can be attributed to diabatic processes. A further motivation for the present study is that downstream impacts of heating on tropopause structures (e.g. Grams *et al.*, 2011) have been implicated in systematic medium-term forecasting issues (e.g. Didone, 2006).

An important aspect of atmospheric models is the need to parametrize water phase transitions. These phase transitions are represented in at least two separate model components. The two main components are often referred to as the cloud microphysics parametrization, which deals with phase transitions due to the thermodynamic state of the model atmosphere at the grid scale, and the convection parametrization, which deals with phase transitions that occur as a result of lifting due to subgrid-scale updraughts which generate cumulus. The cloud microphysics parametrization may also be referred to as the large-scale precipitation parametrization, which is the convention followed here. Depending on the design of the model, phase transitions may also be handled within the boundary-layer turbulence parametrization. There is of course no well-defined equivalent separation of phase transitions in the actual atmosphere.

After a series of experiments across a wide range of model resolutions with the ECMWF model, Jung *et al.* (2012) found that that in the Extratropics the mean convective precipitation was hardly modified while large-scale precipitation slightly increased so that the ratio convective to large-scale precipitation decreased from 0.918 to 0.854 as resolution increased from T159 to T2047 in the Northern Hemisphere (with slightly different values for the Southern Hemisphere; their Table 3). However, it is worth noting that this model uses a resolution-dependent closure for the convection parametrization, as introduced by Bechtold *et al.* (2008).

In contrast, the precipitation in some other models exhibits strong sensitivities of the parametrization suite to model resolution (e.g. Rauscher *et al.*, 2013). In a mesoscale modelling context, Done *et al.* (2006) demonstrated that the total precipitation was dependent on whether a state of statistical equilibrium held between convection and its large-scale forcing. If statistical equilibrium held, then the total precipitation amount was largely insensitive to the split between resolved and parametrized convection. In contrast, if statistical equilibrium conditions were not met, then the total precipitation simulated was sensitive to that split.

The aims of the current study are to identify the regions of maximal diabatic activity in the vicinity of an extratropical cyclone and to investigate to what extent different parametrized diabatic processes are responsible for that diabatic activity within a numerical weather prediction model. These aims naturally draw our attention to the warm conveyor belt (WCB; Harrold, 1973; Browning, 1990; Eckhardt *et al.*, 2004) given that it is a region of strong ascent, but not exclusively so, and the WCB will be placed into its wider context within the system studied. Diabatic activity will be identified using an accumulative tracer method somewhat similar to that of Stoelinga (1996), but here applied to potential temperature directly. Using this method, the modification of potential temperature can be decomposed into the individual contributing model processes. The tracer method is also complemented by using a trajectory-based analysis in order to reveal the diabatic modifications which take place in within the model in a Lagrangian sense.

The rest of this contribution is organized as follows. A detailed account of the methodology is given in section 2. Section 3 is devoted to a description of the synoptic situation during the case-study. The simulation studied is described and validated in section 4. Its analysis is presented in section 5 in terms of the redistribution of air masses in the vicinity of the cyclone and in terms of the diagnosis of diabatic mechanisms in section 6. In section 7 the effects of the parametrization of convection and the split of latent heating between parametrizations are studied by performing a second simulation with reduced parametrized convection. A summary and conclusions are given in section 8.

2. Methods and methodology

2.1. Model

All the simulations in this study are undertaken with the Met Office Unified Model (MetUM) version 7.3 in its limited-area model configuration. This is a finite-difference model which solves the non-hydrostatic deep-atmosphere dynamical equations with a semi-implicit, semi-Lagrangian integration scheme (Davies *et al.*, 2005). It uses Arakawa C staggering in the horizontal (Arakawa and Lamb, 1977) and is terrain following with a hybrid-height Charney–Phillips (Charney and Phillips, 1953) vertical coordinate. Parametrization of physical processes includes long-wave and short-wave radiation (Edwards and Slingo, 1996), boundary-layer parametrization (Lock *et al.*, 2000), cloud microphysics and large-scale precipitation (Wilson and Ballard, 1999), and convection (based on Gregory and Rowntree, 1990). The convection scheme in the MetUM is a mass-flux scheme with a convective available potential energy (CAPE) time-scale closure for deep convection. The CAPE time-scale determines the rate of consumption of CAPE by convection and thereby determines the intensity of the convection parametrization response to the large-scale forcing. The shallow-convection parametrization is based on the results of Grant and Brown (1999) with a thermodynamic cloud-base closure (Grant, 2001).

The simulations have been performed over the North Atlantic–Europe (NAE) domain. The NAE domain has a horizontal grid spacing of 0.11° and uses a rotated pole so that the grid spacing in distance terms is approximately uniform at ~ 12 km across the domain. It contains 600×360 horizontal grid points and has 70 vertical levels with a lid at around 80 km. The NAE domain extends approximately from 30°N to 70°N in latitude and from 60°W to 40°E in longitude in the non-rotated geographical coordinate system.

2.2. Tracer methods

If the atmosphere was adiabatic, potential temperature (and entropy) would be conserved along trajectories in a Lagrangian framework. However, changes in potential temperature do occur and these in turn influence the atmosphere dynamics. Changes to the dynamics themselves modify the development of diabatic processes closing a feedback loop characterized by strong nonlinearity. The most important diabatic processes in the atmosphere are diabatic turbulent mixing, radiation and water phase transitions associated with latent heat absorption and release.

The method described here is similar to the method for potential vorticity (PV) described in Stoelinga (1996) and Gray (2006) with differences in the formulation to reflect the differences between PV and the variables of interest here. Potential temperature θ can be written in terms of a conserved component θ_0, which can be redistributed by advection but is not modified by parametrized diabatic processes, and a modification component $\Delta\theta$ which is also advected and carries, in addition, the accumulative action of diabatic processes. The modification component can be further decomposed in several sub-terms, each carrying the action of a specific diabatic process. The potential temperature can therefore be written as

$$\theta(x,t) = \theta_0(x,t) + \sum_{i=\text{proc}} \Delta\theta_i(x,t) + R_\theta(x,t), \qquad (1)$$

where $\Delta\theta_i$ represents the accumulative contribution due to the ith parametrized process. The processes we include in this analysis are:

(i) contribution due to the boundary-layer parametrization, $\Delta\theta_{BL}$;
(ii) contribution due to the large-scale cloud and precipitation (microphysics) parametrization, $\Delta\theta_{mp}$;
(iii) contribution due to the convection parametrization, $\Delta\theta_{conv}$; and
(iv) contribution due to radiation, $\Delta\theta_{rad}$.

The term R_θ represents a residual arising from other sources of potential temperature modification related to fluxes through the boundaries and numerical (interpolation errors) and physical diffusion.

Potential temperature satisfies the transport equation

$$\frac{D\theta}{Dt} = \frac{\partial\theta}{\partial t} + \mathbf{v}\cdot\nabla\theta = \sum_{i=\text{proc}} S_{\theta_i}. \qquad (2)$$

where S_{θ_i} is the source from each diabatic process and $S_{\theta_0} \equiv 0$ by definition.

Substituting Eq. (1) into Eq. (2) and collecting similar terms yields a transport equation for each component of Eq. (1) so that

$$\frac{D\theta_0}{Dt} = \frac{\partial\theta_0}{\partial t} + \mathbf{v}\cdot\nabla\theta_0 = 0, \qquad (3)$$

and

$$\frac{D\Delta\theta_i}{Dt} = \frac{\partial\Delta\theta_i}{\partial t} + \mathbf{v}\cdot\nabla\Delta\theta_i = S_{\theta_i}. \qquad (4)$$

A suitable initial condition for Eq. (3) is to use θ_0 to describe the potential temperature at the start of the model simulation, so that $\theta_0(0) = \theta(0)$. We also set $\Delta\theta_i$ to zero at the initial time for all of the diabatic processes such that these tracers describe the accumulative effect of each source term.

It is clear from Eq. (3) that θ_0 is subject to the action of advection only, whereas Eq. (4) shows that the accumulative tendency tracers are affected by both advection and specific diabatic processes. R_θ also satisfies an equation of this form. However, rather than attempting to formulate it explicitly, it is simpler to compute this as

$$R_\theta = \theta - \theta_0 - \sum_i \Delta\theta_i.$$

Equations (3) and (4) are solved within the model simulation code, and θ_0 and $\Delta\theta_i$ are output as model diagnostics. Parametrization calculations are structured sequentially within the model so the source terms at each timestep can be computed by differencing the potential temperature before and after each parametrization call. The advection terms are computed using the inbuilt model calculations for the advection of tracer fields with a semi-Lagrangian scheme (Davies *et al.*, 2005).

The redistributed initial field θ_0 serves as a labelling field for an air-mass specification. However, its value is not unique and therefore the air-mass specification of the flow field can necessarily only be approximate. Nonetheless, this property of θ_0 is useful when it is plotted on θ levels because it makes immediately obvious the origin of air masses on that level. Values of θ_0 larger (smaller) than θ can be interpreted as indicating an air mass that has undergone cross-isentropic descent (ascent) to reach the θ level in question (section 5).

An analogous approach can be applied to any other advected variable which has source terms that can be decomposed on a process-by-process basis. In particular, we have developed suites of diagnostics for each of the three moisture variables present in the MetUM, namely the specific humidity, q, liquid

water content, q_{cl}, and ice water content, q_{cf}. This enables a further separation of the boundary-layer θ-tracer into two sub-components which would otherwise be impossible to differentiate. Thus, $\Delta\theta_{BL} = \Delta\theta_{BLmix} + \Delta\theta_{BL\,lh}$, where $\Delta\theta_{BLmix}$ is the contribution due to mixing and $\Delta\theta_{BL\,lh}$ is the contribution due to latent heat exchange, both within the boundary layer. The latent heating contribution is determined as

$$\Delta\theta_{BL\,lh} = \frac{L}{c_p}\frac{\Delta q_{cl,BL}}{\Pi}, \qquad (5)$$

where L is the latent heat of condensation, c_p is the specific heat of dry air at constant pressure and $\Pi = (p/p_0)^{R/c_p}$ is the Exner function, where p is pressure, $p_0 = 1000$ hPa is a reference pressure and R is the gas constant for dry air. $\Delta q_{cl,BL}$ is the contribution to change in q_{cl} in the boundary layer. This variable, and therefore $\Delta\theta_{BL\,lh}$, are not subject to surface fluxes in the lowest model level. The use of Eq. (5) assumes that there is no ice cloud within the model boundary layer, a point that we have checked explicitly for the simulations presented here.

It is also convenient to consider the total contribution due to large-scale latent heat exchange, defined as $\Delta\theta_{LS\,lh} = \Delta\theta_{BL\,lh} + \Delta\theta_{mp}$, consolidating the latent heating contributions from the boundary layer and large-scale cloud and precipitation (microphysics) parametrizations. We also define a total latent heat as $\Delta\theta_{lh} = \Delta\theta_{LS\,lh} + \Delta\theta_{conv}$, which includes the contribution from the convection parametrization. (It must be noted, however, that the source term from a convective parametrization actually includes convective transports of sensible heat as well as latent heating effects; Yanai *et al.*, 1973).

2.3.   Trajectory analysis

Our analysis also involves the consideration of trajectory ensembles (e.g. Wernli and Davies, 1997). The ensembles were constructed by computing backward trajectories which arrive at regions exhibiting large accumulated heating ($\Delta\theta > 12.5$ K after 24 h of simulation). As will be shown in section 6, these regions were typically located at upper levels ($315 \lesssim \theta \lesssim 335$ K). Each individual trajectory was computed based on hourly outputs of the model velocity components on each model level, linearly interpolated in both space and time to the appropriate location, and integrated backwards in time for 23 h (between 0600 UTC on 30 September and 0700 UTC on 29 September) using the fourth-order Runge–Kutta method.

Once the trajectories were computed, atmospheric fields such as the pressure, temperature, wind velocity components and θ-tracers were interpolated onto the parcel positions to obtain the evolution of those fields along trajectories. The material rates of change of the fields along trajectories, represented by the operator D/Dt, were computed using centred differences. Thus, rather than being interpreted as an instantaneous value, our results for $D\phi/Dt$ should be interpreted as hourly mean values of the Lagrangian rate of change of quantity ϕ.

In order to study quantities such as $D\Delta\theta_i/Dt$ in a reliable way, it is important to ensure that there is a good level of consistency between the trajectory ensembles, the advection as performed within the model simulation, and the on-line advection calculations for the θ tracers. The θ_0 field has been used to make a test of each of the trajectory calculations. Theoretically, since the θ_0 field is only affected by advection, it will be conserved along trajectories. In practice of course this is not exactly true, because the off-line computation of trajectories does not perfectly reproduce the model advection. Therefore, a useful measure of consistency is to compare the value of θ_0 interpolated to a trajectory arrival point (at 0600 UTC on 30 September) to the initial θ_0 value at the start point (at 0700 UTC on 29 September). Those trajectories which exhibit a departure smaller than a certain threshold are kept for further analysis while the rest are discarded. The chosen threshold value was $|\Delta\theta_0| < 5$ K
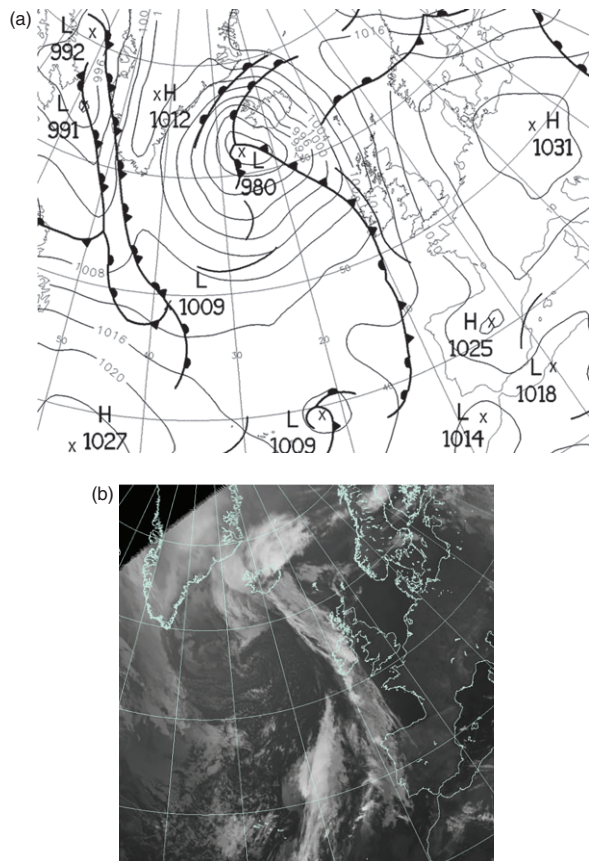
Figure 1. (a) Met Office operational analysis chart (©2011 Crown Copyright) and (b) infrared satellite image valid at 0600 UTC on 30 September 2011 (Courtesy NERC Satellite Receiving Station, Dundee University, Scotland. http://www.sat.dundee.ac.uk/).

Figure 2. Potential temperature (shading) at 300 hPa in (a) the Met Office operational analysis (©2011 Crown Copyright, Met Office) and (b) our 24 h simulation at 0600 UTC on 30 September 2011. Also shown are the 300 hPa 2 PVU contour (bold) and 850 hPa θ_e contours (thin) with a 5 K separation. Black crosses indicate the position of the mean-sea-level low pressure centre.

between the beginning and the end of the simulation, which is comparable to the standard deviation of R_θ at 12.5 km after a 24 h integration. With this threshold value, approximately 66% of the trajectories are retained. The proportion of retained trajectories ranges between 60 and 71% if the threshold value is varied between 4 and 6 K. The results presented here are qualitatively robust to these variations of the threshold value. Rejected trajectories are mainly located in the upper troposphere, where small errors in the location of a parcel translates into large errors in θ due to large θ vertical gradients.

Both the tracer methods and the trajectory analysis, as described in sections 2.2 and 2.3, are designed for the analysis of model behaviour at the resolution of the model and, therefore, no additional assumptions are made regarding sub-grid processes. The grid-scale wind components are used to compute both the on-line advection of variables and tracers in the model and the off-line trajectories. From this point of view, both methods are consistent. In this sense, the workings and details of the parametrization schemes are treated as black boxes, considering only their effects at the grid-scale, in both the model and our diagnostics.

3. Case-study: synoptic situation

The selected case is the low-pressure system shown in Figure 1 which is centred to the southwest of Iceland with a long trailing cold front. The system began its development at around 0600 UTC on 28 September 2011, with a low centre being identified at 43°N, 28°W. From there it travelled predominantly northwards to be located around 62°N, 25°W by 1200 UTC on 30 September 2011, deepening from 997 hPa to 973 hPa in 54 h. The system's trailing cold front reached Ireland around 0600 UTC on 30 September 2011 (Figure 1(a)) and kept travelling eastwards, producing precipitation over the United Kingdom. An infrared satellite image at 0600 UTC on 30 September 2011 (Figure 1(b)) shows the cloud
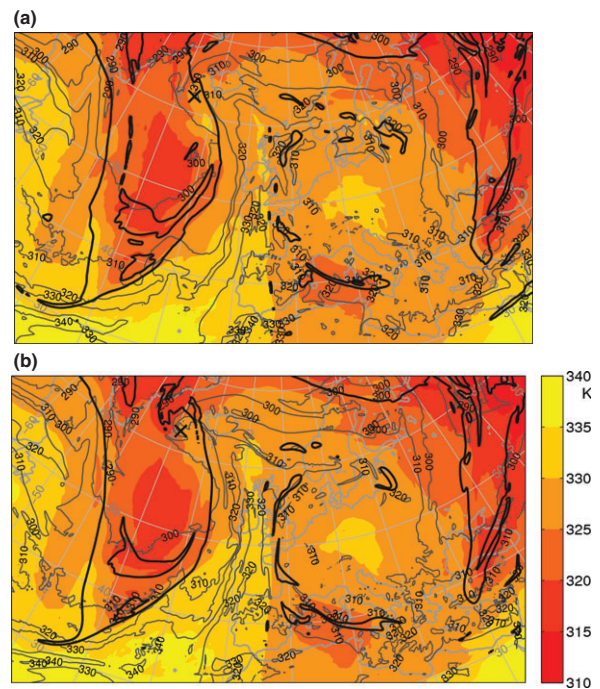
band associated with the cold front. It also shows the T-bone structure indicating a bent-back front in the vicinity of the cyclone's low centre, with a section of high cloud moving to the east and a section of lower cloud weakly wrapping around the low centre.

The numerical simulations were initialized at 0600 UTC on 29 September 2011 from the Met Office operational analysis valid at that time and at the same resolution as the simulation. The lateral boundary conditions used were the operational lateral boundary conditions, provided by the Met Office, valid from 2100 UTC on 28 September for 72 h and updated every 3 h.

4. Validation of the simulation

Figure 2 shows the Met Office analysis valid at 0600 UTC on 30 September 2011 (Figure 2(a)) and our simulation at the same time (Figure 2(b)). It includes the surface low-pressure centre, and lower- (850 hPa θ_e contours) and upper-level fields (300 hPa θ and 2 PVU contours). The frontal structure in both frames is remarkably similar, with the low-level cold front appearing ahead of the upper-level trough. The 300 hPa θ_e field also appears very similar in both frames. Nevertheless, there are a few differences to be noted. In the simulation, the low-pressure centre is located slightly to the west with respect to the analysis. Furthermore the θ_e contours near the low centre are more wrapped up in the simulation than in the analysis and show signs of an incipient warm seclusion. The same characteristic can also be observed at upper levels, where the tropopause (contoured by the 300 hPa 2 PVU contour) in the simulation is more wrapped up in the region directly above the surface low centre. As a consequence, the simulation shows polar air with lower θ_e being advected towards the cyclone centre.

A simulation starting 18 h earlier (at 1200 UTC on 28 September 2011) under otherwise identical conditions was also performed. This produced much bigger departures from the analysis. The main differences were again found in the structure of the tropopause at 300 hPa above the low centre. The simulation exhibited a tropopause which had completely wrapped up around the cyclone centre, whereas the tropopause remained to the east of the cyclone centre at all times in the Met Office analysis (e.g. Figure 2(a)). This is an example of errors often found in numerical
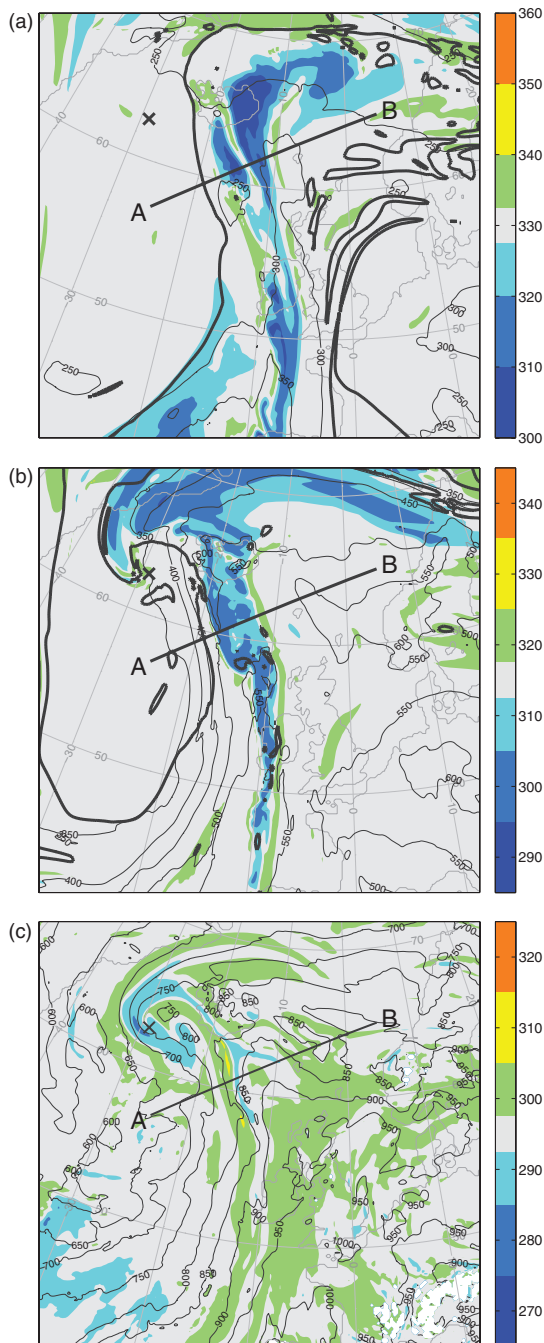
Figure 3. Horizontal sections of θ_0 (K) at 0600 UTC on 30 September 2011 at (a) 330 K, (b) 315 K and (c) 295 K. Thin black contours represent isobars with a separation of 50 hPa, and bold black contours in (a) and (b) represent the 2 PVU contour. Both sets of contours are plotted on the specified θ level. The line segments AB mark the position of the vertical section shown in Figure 7. Black crosses indicate the position of the mean-sea-level low pressure centre. The colour scale in each panel is centred around the value of the θ surface.

weather forecasts regarding the downstream ridge (Dirren *et al.*, 2003).

5. Air-mass redistribution

In this section the θ_0 tracer is used to infer the redistribution of air masses in the vicinity of the cyclone centre. Figure 3 shows this tracer field at three different θ-levels: 330, 315 and 295 K. The colour scale has been chosen so that the panels highlight the isentropic level of air masses at the start of the simulation (24 h beforehand). Cold shades indicate air which was originally found at lower potential temperature levels while warm colours indicate air from upper levels.

The 330 K level (Figure 3(a)) is an almost flat surface ($250 < p < 300$ hPa). The 2 PVU contour, indicating the intersection

of the tropopause and the θ-level, shows the main upper-level ridge to the east of the cyclone's centre and indeed to the east of the system's cold front. There is a cold anomaly on the tropospheric side of the ridge, indicating an air mass that had its origin at lower levels ($\theta < 327.5$ K). The cold anomaly extends upwards in a bubble-like intrusion of tropospheric air, reaching pressure levels, $p < 200$ hPa (also Figure 7(a)). The core of this air mass exhibits values of $\theta_0 < 310$ K, normally corresponding to pressures of around 600 hPa. There are also scattered regions of subsided air ($332.5 < \theta_0 < 340$ K) along and around the regions of ascent.

The system's cold front can be appreciated at 315 K (Figure 3(b)), as this θ-surface slopes down from around 350 hPa to around 500 hPa. The system's warm front is similarly apparent at this level to the east of the cyclone centre. The 2 PVU contour marks the location of the main upper-level ridge, and in this simulation part of the ridge is wrapping around the cyclone's centre. A cold-anomaly band is found on the tropospheric side of the 2 PVU contour, with $\theta_0 < 312.5$ K. The air masses which were subject to the largest cross-isentropic ascent were originally located at $\theta < 305$ K (i.e. around 700 hPa). The location of the cold-anomaly band (to the east of the western flank of the upper-level ridge, with more pronounced ascent as it approaches the warm front near the cyclone centre) is consistent with the features expected in the system's WCB. There is also a narrow band of weakly anomalous warm air, indicating weak cross-isentropic subsidence ($317.5 < \theta_0 < 325$ K), on the warm sector side of the WCB at this level.

Since the system is already in its mature stage, the surface cold front is weaker than that at mid levels. Thus, the θ-surface at 295 K (Figure 3(c)) slopes more gently than at levels above, although the front still spans pressure layers from 600 to 950 hPa. On the 295 K surface, subsidence ($\theta_0 > 297.5$ K) is more widespread across the warm sector, while there are intermingled regions of weak cross-isentropic ascent and descent behind the cold front corresponding to shallow convective activity in the region. There is slightly stronger cross-isentropic ascent ($\theta_0 < 285$ K) near the cyclone centre, possibly as part of the system's cold conveyor belt (Carlson, 1980; Schultz, 2001).

6. Attribution of features by process

The accumulative action of all parametrized diabatic processes is described by departures of θ_0 from the corresponding θ-surface value in Figure 3. The redistribution of θ_0 on the 330 K surface shows that there was important accumulative heating in tropospheric air reaching the tropopause as an extension of the system's WCB (Figure 3(a)). Figure 4 shows the contributions of individual diabatic processes in the θ-decomposition at 330 K, corresponding to Figure 3(a).

The most important contribution in the region of the tropospheric air mass that reaches the tropopause is the large-scale latent heating (Figure 4(a)), for which $\Delta\theta_{\mathrm{LS\,lh}} > 10$ K at the end of the 24 h simulation. The convection parametrization is the second main contributor to the potential warming of this region (Figure 4(b)), with $0.5 < \Delta\theta_{\mathrm{conv}} < 10$ K for much of the region and small areas in which $\Delta\theta_{\mathrm{conv}} > 10$ K. Radiation (Figure 4(c)), mainly long-wave radiation, produces weak widespread cooling. Such cooling is at its strongest along the south-to-north portion of the WCB, corresponding to radiative cooling at the top of the cloud band that constitutes the WCB. The weak cross-isentropic descent seen in Figure 3(a) along the outer rim of the WCB, especially on its cold side, is mainly due to the cooling produced by the radiation scheme in regions where this effect is not totally overcome by the action of latent heating. The residual term R_θ is at its largest at upper levels because the strong winds there are able to advect contributions to potential temperature arising from the boundary conditions into the simulation domain (Figure 4(d)). At lower levels ($290 < \theta < 330$ K) and for the time under examination here (T + 24), R_θ is small enough to be
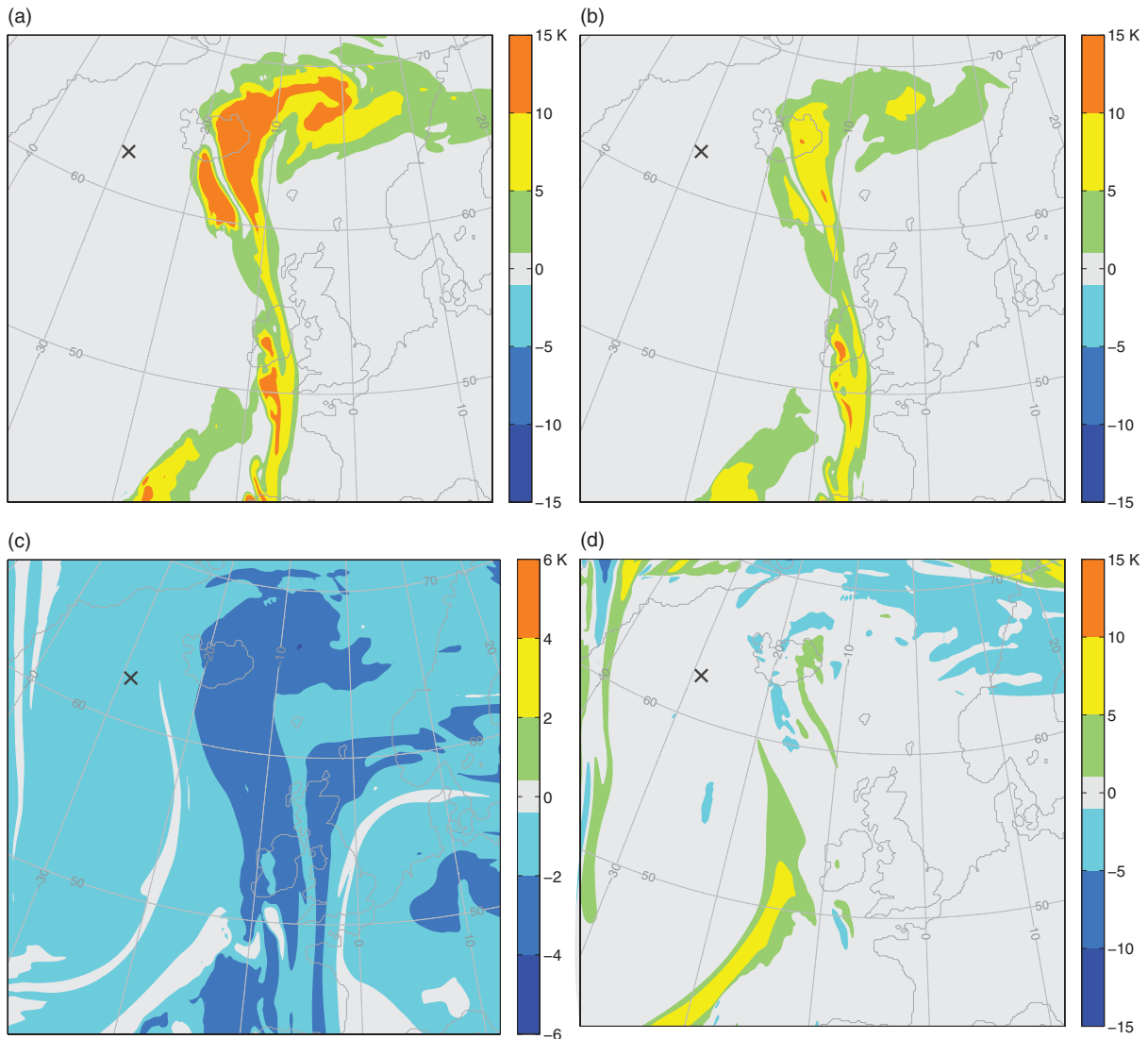
Figure 4. Parametrized diabatic process θ-decomposition at $\theta = 330$ K at 0600 UTC on 30 September 2011: (a) $\Delta\theta_{LS\,lh}$, (b) $\Delta\theta_{conv}$, (c) $\Delta\theta_{rad}$ (notice the different colour scale) and (d) R_θ. Black crosses indicate the position of the mean-sea-level low pressure centre.

neglected in comparison with the effects of the main diabatic processes. It is important for our methods and the interpretations that the presence of the residual term (mainly emanating from the lateral boundaries) should be monitored, especially in the case of longer-term simulations.

At the 315 K level, the region of anomalous θ_0 marks out the position of the WCB (Figure 3(b)). As shown on Figure 5, the most important contribution at this level is again the large-scale latent heating ($\Delta\theta_{LS\,lh} > 10$ K; Figure 5(a)). The accumulative effects of large-scale latent heating extend all the way from the south to the north along the main portion of the WCB and then along the tropospheric side of the the upper-level ridge, including the extrusion that wraps around the cyclone centre. Moreover, large-scale latent cooling is also responsible for the band of weak cross-isentropic subsidence on the warm sector side of the WCB. The second most important contribution is due to the convection parametrization (Figure 5(b)). This contribution is concentrated along the main portion of the WCB before the airstream splits into primary (anticyclonic) and secondary (cyclonic) branches. Radiation (Figure 5(c)) is the third contributor, with widespread cooling somewhat concentrated around the wrapping-up extrusion around the cyclone centre. It has been pointed out previously (section 4) that this extrusion did not appear in the Met Office analysis and therefore it might not have occurred in reality. The results shown here indicate that the processes whose action accumulates within this feature are large-scale latent heating (with some contribution from the convection parametrization) and radiation.

Closer to the surface, the redistribution of air masses is characterized by intermingled weak cross-isentropic ascent and descent behind the cold front and widespread weak cross-isentropic descent in the warm sector. Large-scale latent heating is the main contributor to the changes in θ along the near-surface cold front on the 295 K surface (Figure 6), strengthening the front by providing a warming band on the front's eastern flank ($\Delta\theta_{LS\,lh} > 10$ K) and a cooling to the west behind the front ($\Delta\theta_{LS\,lh} < -10$ K; Figure 6(a)). The warming band is formed by latent heat release due to condensation whereas the cooling band is formed by the evaporation of precipitation behind the cold front (Joos and Wernli, 2012). As expected, cross-isentropic ascent in the wider region behind the cold front occurs due to the convection parametrization; this is most evident towards the lower left corner of Figure 6(b). Radiation is responsible for widespread cooling and, as a result, weak cross-isentropic descent within the domain at this level (Figure 6(c)). Mixing produced by boundary-layer turbulence is an important contribution only for levels close to the surface. In this case, its main contribution is found along the near-surface cold front which can be explained by the enhanced turbulent mixing expected in such a region of enhanced wind convergence (Figure 6(d)).

6.1. Vertical structure

Figure 7 shows the vertical extent of the features discussed so far in vertical sections along the segment AB, defined in Figure 3. Figure 7(a) shows θ_0, and the differences between the contours
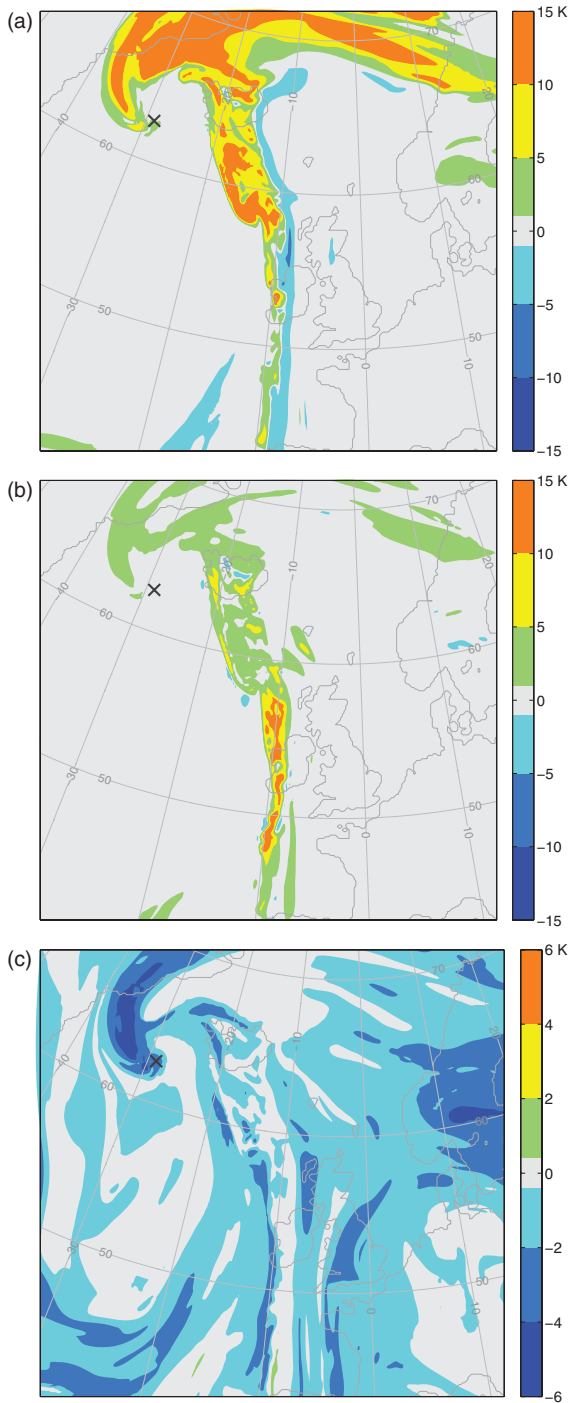
Figure 5. Parametrized diabatic process θ-decomposition at $\theta = 315$ K at 0600 UTC on 30 September 2011: (a) $\Delta\theta_{\mathrm{LS\,lh}}$, (b) $\Delta\theta_{\mathrm{conv}}$ and (c) $\Delta\theta_{\mathrm{rad}}$ (notice the different colour scale). Black crosses indicate the position of the mean-sea-level low pressure centre.

and colours on that panel can be interpreted as total accumulative heating over the preceding 24 h. The most prominent feature in this panel is the strong cross-isentropic ascent between $20°$W and $10°$W, extending from near-surface levels (~ 800 hPa) to around 200 hPa. Much of the air reaching higher isentropic levels has come from a layer extending between 290 and 320 K. The ascended air within this section seems to be somewhat separated into an upper region above $\theta = 325$ K and a lower region below $\theta = 320$ K. In the upper region, air originating at levels as low as $\theta < 300$ K (corresponding to pressures $p < 800$ hPa) has reached levels between 325 and 335 K ($250 < p < 350$ hPa) over the course of 24 h. This upper region is clearly part of the cold anomaly on the 330 K surface (Figure 3(a)) which was discussed previously. In the lower region, the ascending air from $\theta_0 < 300$ K has reached levels between 315 and 320 K ($400 < p < 500$ hPa) during the same interval. This region constitutes part of the cold

anomaly band which can be found along the tropospheric side of the upper-level ridge (Figure 3(b)). Despite the differences in the ascent rates for these two sections, both are consistent with common criteria used to identify WCBs through trajectory analysis (e.g. Eckhardt *et al.*, 2004). The localized strong ascent just described is compensated by widespread weak tropospheric subsidence.

The θ-decomposition explains the vertical structure just described. Figure 7(b) shows the contribution due to large-scale latent heating. This is responsible for most of the total accumulated heating in both the upper and lower ascending regions ($\Delta\theta_{\mathrm{LS\,lh}} > 10$ K). This panel also shows how the parametrizations of large-scale latent heat processes produce cooling and cross-isentropic subsidence behind the cold front at lower levels ($p > 600$ hPa), due to the evaporation of raindrops and the sublimation and melting of ice and snow as they fall through layers of drier air.

The regions where there is a large accumulated contribution from the convection parametrization are more restricted than those with large contributions due to large-scale latent heating (Figure 7(c)). Below ~ 400 hPa, $1 < \Delta\theta_{\mathrm{conv}} < 10$ K, but there are stronger contributions at upper levels where $\Delta\theta_{\mathrm{conv}} > 10$ K. The $\Delta\theta_{\mathrm{conv}}$ contributions at upper levels enable low θ_0 air masses to reach higher isentropic levels. Indeed, the sum of contributions from large-scale latent heating and convection together reproduces very well the pattern exhibited by total diabatic heating $\Delta\theta = \theta - \theta_0$ (not shown). Radiation is responsible for the widespread cross-isentropic subsidence elsewhere within the troposphere (Figure 7(d)). It is also responsible for some additional cooling near to the surface, especially to the east of the vertical section, within the cyclone's warm sector. As expected, stratospheric air is not strongly acted upon by any of the parametrized processes, leaving the stratospheric air largely undisturbed.

7. Balance between processes

Accumulated diabatic changes in the lower region of the vertical cross-section AB are mainly due to large-scale latent heating. However, in the upper region parametrized convection provides additional heating which allows this air mass to reach higher isentropic levels. In order to investigate further the action of convection in the vicinity of the cold front and the WCB, a simulation was performed with reduced parametrized convection. A reduced strength of convection was achieved by increasing the CAPE closure time-scale, specifically increasing it from the standard value of 1 800 s to 15 000 s. This value was chosen to reduce the strength of convection yet to maintain the model's numerical stability without the need to retune parameters in other parametrization schemes. From here onwards, the simulation with standard parametrized convection settings is labelled STDCON, whereas the simulation with reduced parametrized convection is labelled REDCON.

Figure 8 shows the evolution of the convective rain rate, the large-scale rain rate and the total precipitation rate in STDCON and REDCON, spatially integrated over an area of 1500 km radius centred on the low-pressure centre. The convective rain rate in REDCON is around half that in STDCON throughout, demonstrating that the increased closure time-scale was indeed successful in reducing the action of parametrized convection. However, the total precipitation rate is similar in both simulations with a maximum difference of about 9% relative to STDCON. The REDCON simulations exhibits stronger time variations, such that its precipitation rate is higher at the beginning and end of the 24 h simulation but lower in the middle part of the simulation. The spatial distribution of precipitation rate is similar in both simulations at all times (not shown). These results suggest that, while the total amount of precipitation due to the cyclone was mainly determined by the moisture supply into the WCB, the partition of precipitation between the convection parametrization
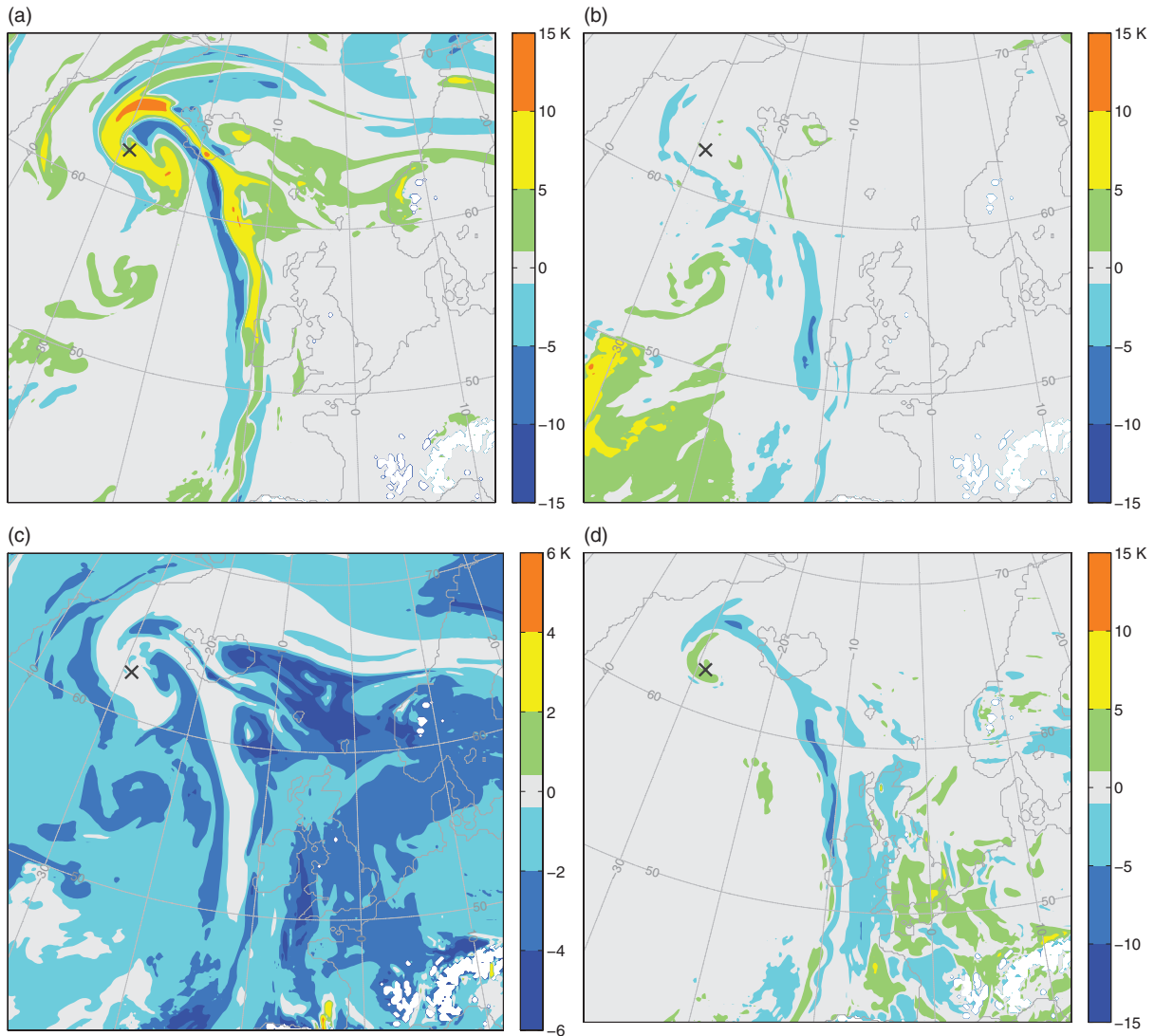
Figure 6. Parametrized diabatic process θ-decomposition at $\theta = 295$ K at 0600 UTC on 30 September 2011: (a) $\Delta\theta_{LS\,lh}$, (b) $\Delta\theta_{conv}$, (c) $\Delta\theta_{rad}$ (notice the different colour scale) and (d) $\Delta\theta_{BLmix}$. Black crosses indicate the position of the mean-sea-level low pressure centre.

and the large-scale cloud scheme depends on the details of the interaction between both schemes. These details, in turn, depend on the formulation and tuning of the parametrization schemes. Similar conclusions have been found by Done *et al.* (2006) and more recently in a study in which two different convection parametrization schemes were used (Martínez-Alvarado *et al.*, 2013).

Despite the similarities in precipitation between the two simulations, there are clear differences in the spatial heating patterns, especially at upper levels. Figure 9 shows the θ_0 field in REDCON at the same levels as in the corresponding Figure 3 for STDCON to which it should be compared. Figure 9 also shows the difference in θ_0 between the two simulations (STDCON−REDCON) at the same isentropic levels. Of course, the main differences are to be expected in those regions where the action of the convection parametrization is most important during the 24 h of STDCON. Indeed, clear differences are found at the 330 K level (Figure 9(a)) in approximately the area of the upper region of the ascending WCB. There is a relatively localized cold anomaly ($\theta_0 < 310$ K) between 55°N and 65°N in approximately the same region occupied by an elongated and unbroken cold anomaly in STDCON. The difference between STDCON and REDCON at this level (Figure 9(d)) shows a south−north wave-like pattern broadly parallel to the west flank of the upper-level ridge. The localized cold anomaly between 55°N and 65°N in REDCON (Figure 9(a)) is collocated with the most prominent crest in the difference wave-like pattern (Figure 9(d)). These features (cold anomaly/crest) can then

be interpreted as localized enhanced ascent in REDCON with respect to STDCON. The 2 PVU contours at this level from the two simulations also show that the difference between STDCON and REDCON has the structure of a wave (Figure 9(d)). This structure is only present on the west flank of the ridge, with other parts of the upper-level wave being almost identical between the two simulations. Differences between Figures 3 and 9 are less noticeable at lower levels. The θ_0 field on the 315 K surface appears very similar in the two simulations to the north of 55°N (Figure 9(b)). At this level, the differences between STDCON and REDCON give rise to a more uniform pattern of negative values which imply that air has been subject to less ascent in REDCON than in STDCON (Figure 9(e)). Moreover, at this level the difference in the 2 PVU contour position between the two simulations is much less noticeable than at 330 K. Near the surface, at the 295 K level, differences in the θ_0 field are more modest than at upper levels (Figure 9(c)). The small differences are located along the cold front where the convection parametrization scheme would be most active in this model (Figure 9(f)).

Figure 10(a) shows a vertical section of θ_0 from REDCON along the segment AB in Figure 9 (at the same location as segment AB in Figure 3). This can be compared with Figure 7 for STDCON. The general similarity between Figures 7(a) and 10(a) is remarkable, although there are differences in the details which deserve comment. The position of the front is essentially the same in both simulations as well as that of the diabatically modified air masses. However, the core of the upper region of the ascending
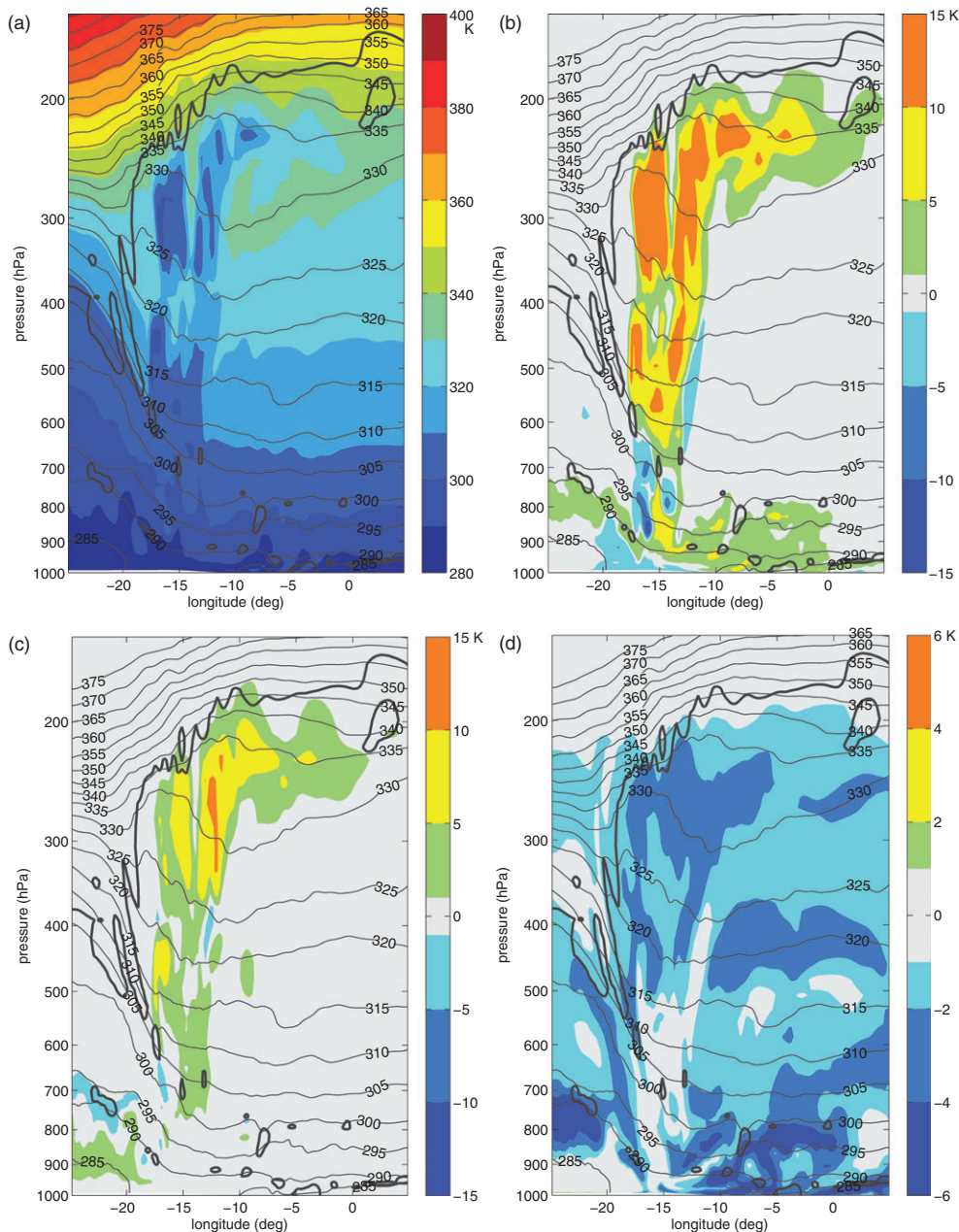
Figure 7. Vertical section along the segment AB indicated in Figure 3 for 0600 UTC on 30 September 2011 showing (a) θ_0, (b) $\Delta\theta_{LS\,lh}$, (c) $\Delta\theta_{conv}$ and (d) $\Delta\theta_{rad}$. Note the different colour scales used. Bold black lines represent the 2 PVU contour. Thin black lines represent potential temperature contours with a 5 K separation.
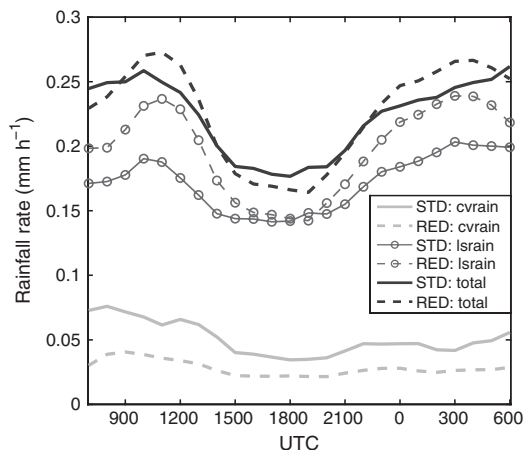

Figure 8. Spatially integrated rain rates for the simulations STDCON (solid lines) and REDCON (dashed lines with circles) from 0600 UTC on 29 September 2011 to 0600 UTC on 30 September 2011. The integrations covered a 1500 km radius area centred on the low-pressure centre. The contributions are shown from convective rain (cvrain; grey lines) and large-scale rain (lsrain; thin lines) to the total precipitation rate (total; bold lines).

WCB in REDCON ($\theta_0 < 310$ K) rises to lower pressures and higher θ levels than in STDCON. The position of the tropopause is also located at slightly higher isentropic levels (by about 5 K) than that in STDCON. Figure 10(b) shows the accumulation of large-scale latent heating in REDCON on the same vertical section. Not surprisingly, the large-scale latent heating is the dominant process responsible for most of the accumulative heating and therefore for most of the cross-isentropic ascent in this case. The accumulative heating due to the convection parametrization in REDCON is at least ten times smaller than it is in STDCON (not shown).

In order to investigate further the origin of the air masses constituting the upper region of the ascending WCB in both simulations, as well as the heating evolution of these air masses, backward-trajectory ensembles were computed. The arrival region was chosen so that it contained the most important differences between the two simulations at upper levels at the arrival time of 0600 UTC on 30 September 2011. Thus, the region was delimited by a box with its opposite corners at 58°N, 20°W and 65°N, 10°W, and extending in the vertical from the 500 hPa pressure level. The parcels were released from every model grid point in the selected box to ensure even spacing within the box.
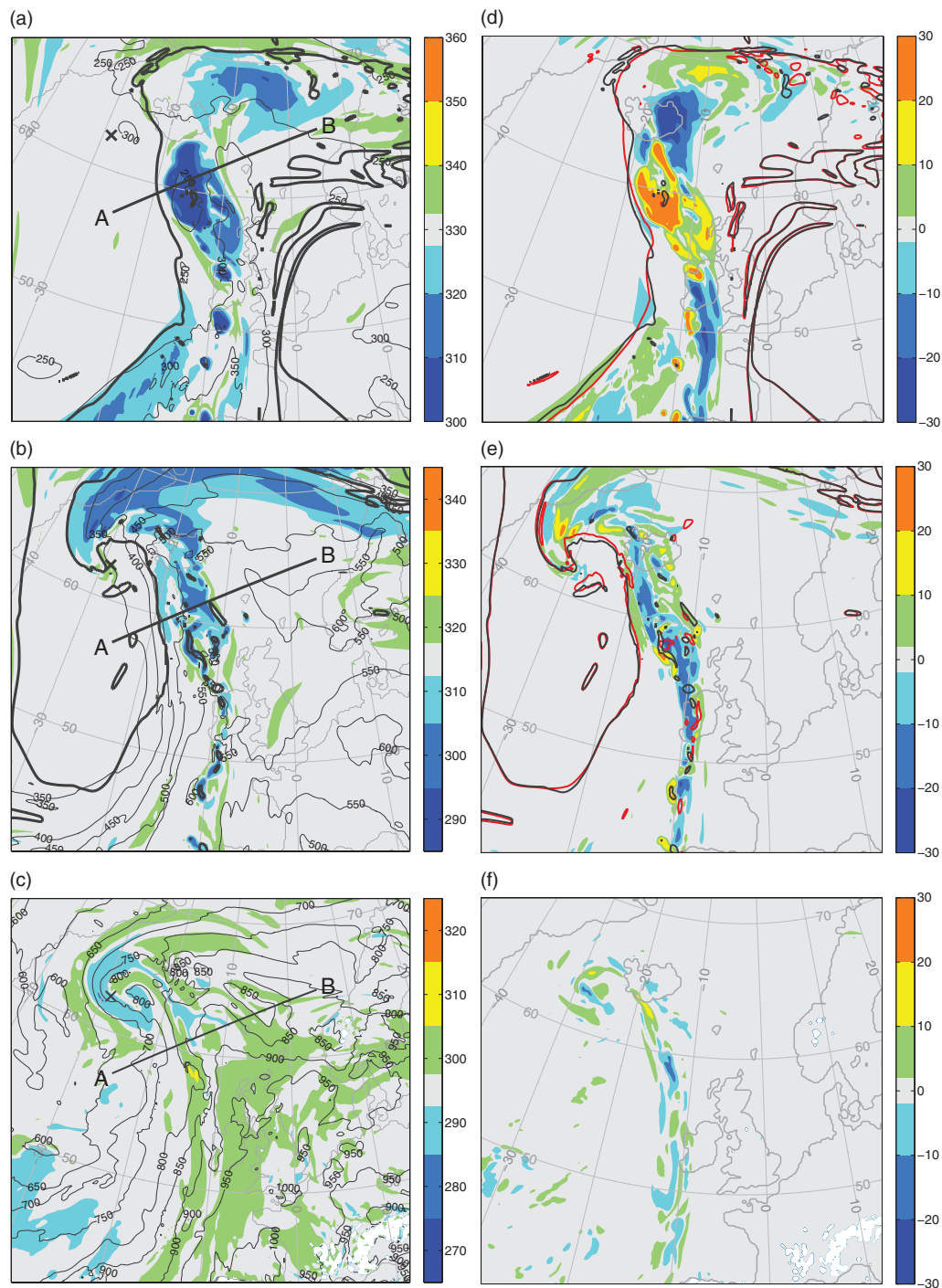
Figure 9. (a–c) As Figure 3, but for the simulation REDCON. (d–f) show θ_0 difference plots (STDCON−REDCON, K) at (d) 330 K, (e) 315 K and (f) 295 K. (d, e) also show the 2 PVU contour in STDCON (red line) and REDCON (black line).

As indicated in section 2.3, a further selection constraint was applied to the trajectories so that only those satisfying $\Delta\theta > 12.5$ K were considered.

Figure 11 shows the evolution along trajectories of the pressure and the heating rates in both simulations. In both cases, the WCB ascent is largely moist-adiabatic, so that the equivalent potential temperature is conserved to within 10 K for around 90% of the trajectories (not shown). When assessed purely on the behaviour of the median, the simulations appear similar with most of the ascent taking place in the last 9 h of integration. However, inspection of the ascent of individual trajectories shows clear differences between the simulations, as is apparent in the 95th percentile. The trajectories which reach the highest levels appear to ascend more gradually and continuously in STDCON (Figure 11(a)) than in REDCON (Figure 11(b)). Furthermore, trajectories between the 25th and 75th percentiles reach higher altitudes in STDCON ($7100 < z < 9500$ m) than in STDCON

($6900 < z < 9100$ m), consistent with the comparison of vertical sections (Figures 7(a) and 10(a)).

This behaviour can be explained in terms of the heating rate along the trajectories. In STDCON the heating is considerable for some of the trajectories in the first half of the simulation, although many more trajectories are subject to somewhat stronger heating during the last 9 h (Figure 11(c)). In contrast, the heating rates in REDCON (Figure 11(d)) remain low for almost all trajectories for the first 12 h of the simulation, and the heating only becomes important after 1800 UTC on 29 September. The decomposition by process confirms that the main contributors to the heating rate in STDCON are large-scale latent heating (Figure 11(e)) and parametrized convection (Figure 11(g)). By design, only the large-scale latent heating is important in REDCON (Figure 11(f)): the contribution from convection remains below 1 K h^{-1} throughout this simulation (not shown). These results indicate that the convection parametrization is acting as a regulating process
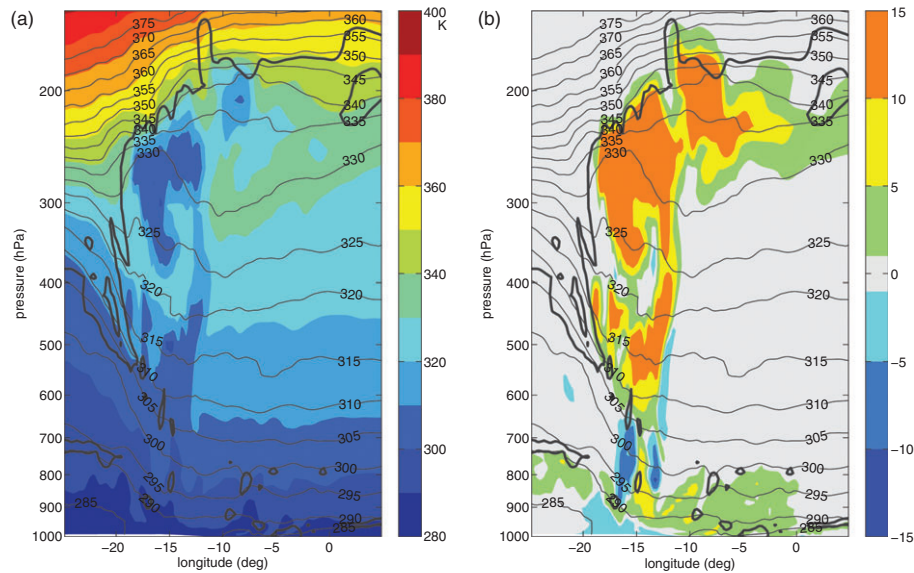
Figure 10. Vertical section along the segment AB indicated in Figure 9 for 0600 UTC on 30 September 2011 showing (a) θ_0 and (b) $\Delta\theta_{LS\,lh}$ for the simulation REDCON. Bold black lines represent the 2 PVU contour. Thin black lines represent potential temperature contours with a 5 K separation.

for large-scale latent heating by gradually releasing the CAPE in the way described by Done *et al.* (2006), for example. A similar mechanism has also been hypothesized in the case of slantwise convection due to moist symmetric instability (Lindstrom and Nordeng, 1992; Gray *et al.*, 2011). In that case, given that current numerical weather prediction models tend not to include a slantwise convective parametrization, moist symmetric instability will be unrealistically released by the cloud microphysics parametrization unless the resolution of the model is sufficient to explicitly resolve slantwise convection.

In Figure 12 we study the relationship within the model between the parametrized heating and the ascent rate. The panels of Figure 12 shows scatter plots of Dz/Dt, the rate of change of height along trajectories, versus the various heating rates. These scatter plots were constructed by plotting every data pair within every trajectory regardless of the time of occurrence. Linear correlations as well as corresponding linear regression models between ascent rate have been computed and are shown on the panels. The relations between ascent rate and heating from radiation, or mixing in the boundary layer are very weak and are not shown.

The total heating rate $D\theta/Dt$ exhibits strong correlation with ascent in both simulations ($\rho > 0.95$, Figure 12(a) and (e)) and linear regression models explain these correlations well. The most noticeable difference between STDCON and REDCON is in the range of the ascent and heating rates, REDCON exhibiting greater values consistently with Figure 11. A subtle difference between simulations is found in the values of α so that for every K of heating, trajectories in REDCON rise 22 m more than in STDCON.

Although the correlation between the large-scale latent heating rate $D\Delta\theta_{LS\,lh}/Dt$ and the ascent rate Dz/Dt in STDCON is strong ($\rho = 0.87$), the inclusion of parametrized convection in $D\Delta\theta_{lh}/Dt$ brings the value of ρ close to its value for total heating rate. Furthermore, the decomposition shows that the convective and large-scale latent heating processes tend to offset each other to an extent, since the proportionality constants of the linear models are larger when each process is considered separately. Specifically $\alpha = 325\,\mathrm{m\,K^{-1}}$ for parametrized convection (Figure 12(b)) and $\alpha = 249\,\mathrm{m\,K^{-1}}$ for large-scale latent heating (Figure 12(c)), whereas $\alpha = 222\,\mathrm{m\,K^{-1}}$ for the combination of the two. When the parametrized convection and large-scale latent heat exchange are considered together, the resulting correlation and regression model are similar to those obtained from the total heating rate (cf. Figure 12(a) and (d)). In the REDCON simulation, the linear regression model corresponding to total heating rate (Figure 12(e)) is also very similar to the linear regression model

between $D\Delta\theta_{lh}/Dt$ and Dz/Dt (Figure 12(h)). Unsurprisingly this is explained to a large extent by $D\Delta\theta_{LS\,lh}/Dt$ (Figure 12(g)) although $D\Delta\theta_{conv}/Dt$ (Figure 12(f)) seems to also provide a small contribution.

The results in this section show that parametrized convection modulates the action of large-scale latent heating and vice versa. The results also show that the processes producing water phase transitions almost completely explain the full relation between heating and ascent in the model.

8. Summary and conclusions

A suite of potential temperature tracers has been produced which decomposes this quantity into a conserved component produced by advection of the initial state, components which each describe the accumulated heating produced by a parametrized model process, and a residual component dominated by the lateral boundaries. These tracers have been used to investigate the roles and interactions of diabatic processes as simulated via parametrization schemes in a numerical model. An important feature of the tracer analysis is the use of the conserved component θ_0 which can be plotted on θ surfaces to identify distinct air masses and to track their displacement in an approximate Lagrangian specification of the flow field.

Trajectory analysis was used in conjunction with the θ-tracers to determine the timing and, by extension, the location where diabatic processes became important. The analysis presented in this study focuses on a 24 h period in the vicinity of a mature extratropical cyclone. Simulations have been performed using two different settings of the convection parametrization scheme: STDCON corresponds to its standard settings scheme as used operationally by the Met Office, whilst in REDCON the response of the scheme to large-scale convective forcing is deliberately weakened.

The most important parametrized diabatic processes in the lower troposphere are radiative cooling and parametrized shallow convection, except that close to the surface cold front both large-scale latent heating and boundary-layer mixing become predominant. Above the surface cold front, ascent within the WCB is accompanied by latent heat release, and this is dealt with mainly by parametrized large-scale latent heating. Likewise, evaporative cooling due to the evaporation of precipitation immediately behind the surface cold front is produced by this same parametrization. These two effects form contiguous bands of accumulated heating and cooling along the front.
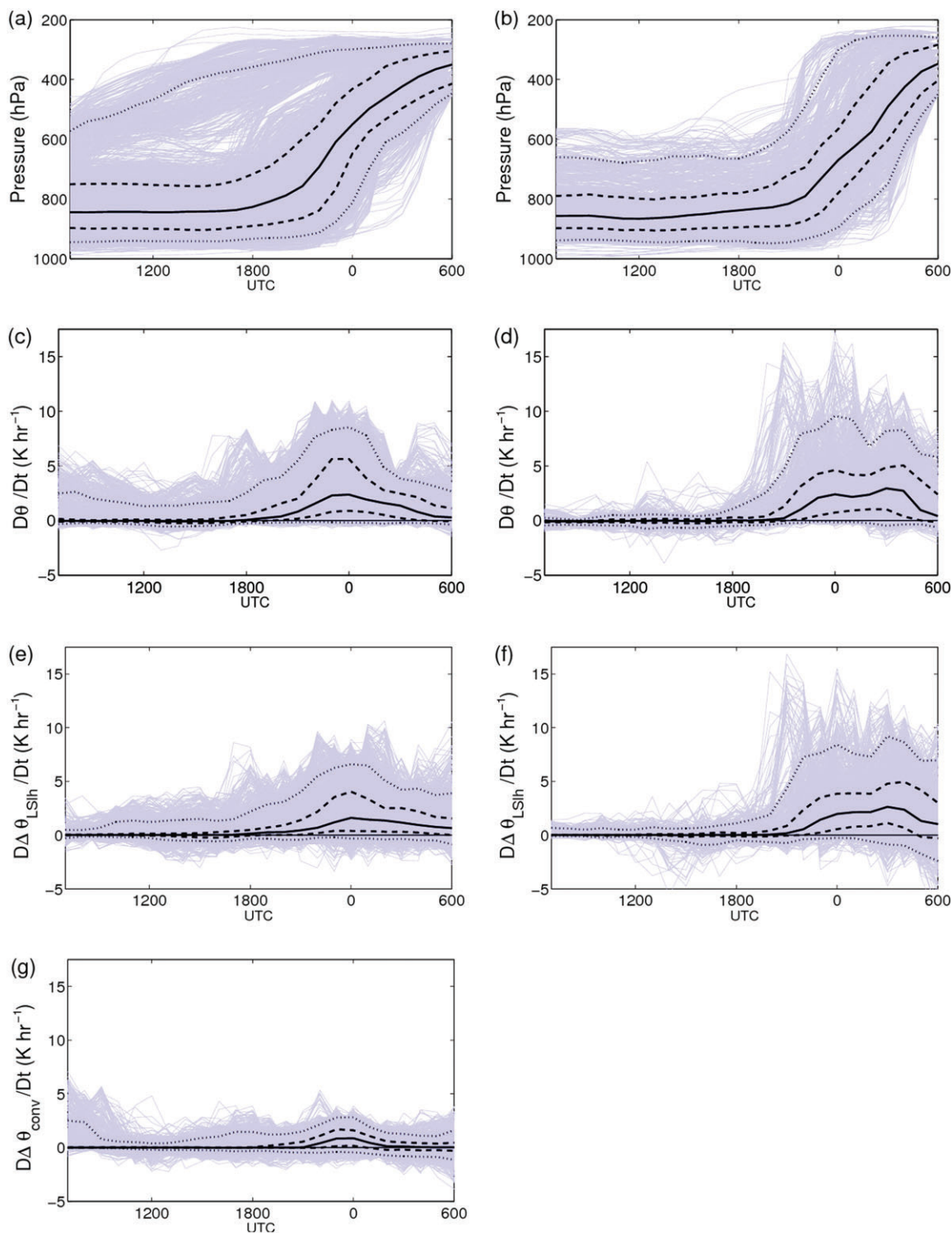
Figure 11. Evolution along trajectories of (a, b) pressure (hPa), (c, d) $D\Delta\theta/Dt$, (e, f) $D\Delta\theta_{LS\,lh}/Dt$ and (g) $D\Delta\theta_{conv}/Dt$ for the simulations (a, c, e, g) STDCON and (b, d, f) REDCON. In each case the solid lines represent the median; dashed lines represent the 25th and 75th percentiles; and, dotted lines represent the 5th and 95th percentiles of the trajectory ensemble. Light grey lines represent individual trajectories within the ensemble. This figure is available in colour online at wileyonlinelibrary.com/journal/qj

At upper levels, the accumulative contributions due to large-scale latent heating and parametrized convection explain most of the diabatic activity. Comparison of our simulations with the operational Met Office analysis shows a tropospheric extrusion wrapping around the cyclone centre might not have happened at the analysis time. This feature also appeared in the simulation with reduced parametrized convection.

The strongest diabatic activity occurred within the WCB and a tropospheric air mass displacing stratospheric air upwards which was also linked to the WCB. On analysis of the vertical structure of diabatic effects through the θ-tracers, it was found that in this particular system the ascending air formed by the WCB air stream consisted of two somewhat distinct regions at

different vertical levels. In STDCON, air within the higher of these regions was found to have experienced additional heating from parametrized convection. Despite this point, the upper region in REDCON extended to higher altitudes. This indicates that the release of CAPE by the convection parametrization regulates the action of large-scale latent heating. Indeed, trajectory analysis has shown that, with reduced parametrized convection, large-scale latent heating tends to eliminate convectively unstable regions in an abrupt manner. The isentropic level reached by ascending air masses within the WCB is important because the associated heating effects at upper levels are accompanied by PV anomalies and hence modification of the tropopause structure
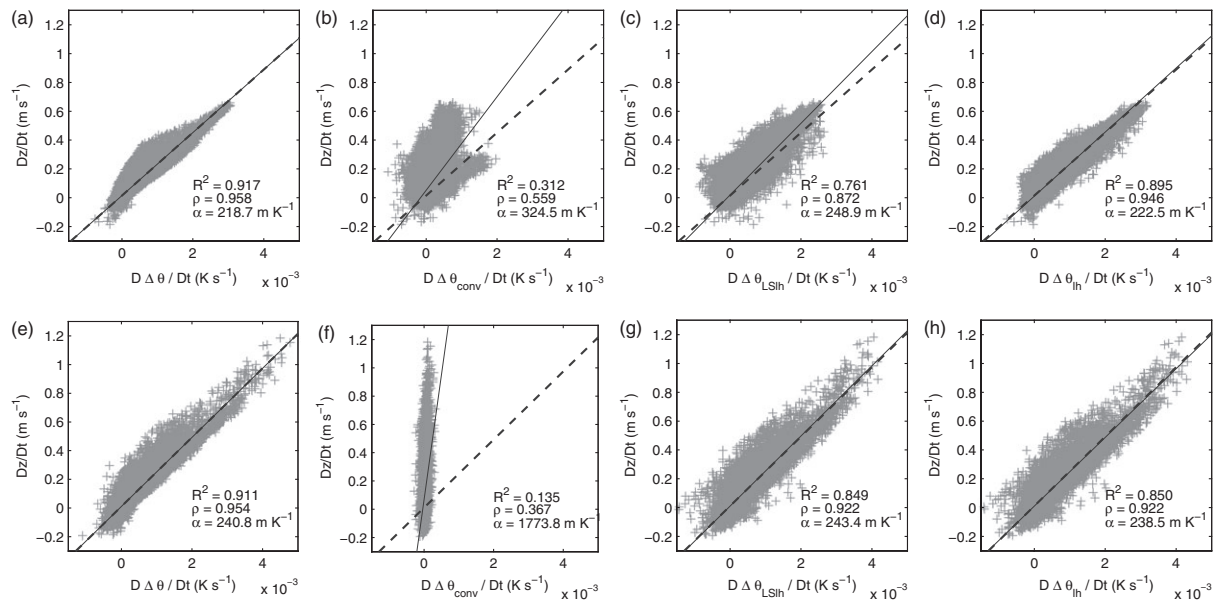
Figure 12. Scatter plots and linear regression models between the trajectory ascent rate (Dz/Dt) and (a, e) $D\Delta\theta/Dt$, (b, f) $D\Delta\theta_{conv}/Dt$, (c, g) $D\Delta\theta_{LSlh}/Dt$ and (d, h) $D\Delta\theta_{lh}/Dt$. Results for the STDCON simulation are plotted in (a–d) and those for the REDCON simulation are plotted in (e–h). Bold dashed lines represents the linear regression model for the total heating rate $D\Delta\theta/Dt$ while thin solid lines represent the linear regression model for the data shown in each panel. The values of the correlation coefficient ρ, the coefficient of determination R^2 and the proportionality constant α for each linear model are also shown.

(e.g. Grams *et al.*, 2011; Joos and Wernli, 2012; Chagnon *et al.*, 2013; Martínez-Alvarado *et al.*, 2013).

The differences between the STDCON and REDCON simulations were restricted to those regions where the accumulative contribution due to parametrized convection is important. Although the differences in the tropopause structure after 24 h are rather modest, it would be very interesting to investigate whether such differences between simulations produce divergent behaviours in longer-term simulations. We did attempt a longer simulation of this case in order to look for any important downstream impacts. These did not occur, but that fact was likely to be due to the limited-area character of our simulations and the fact that the WCB was already approaching the northern boundary of the domain; the constraining effect of lateral boundary conditions will have forced the simulations to remain close together.

Although our results here have been presented as a case-study analysis, it may be noted that we have examined other cases using the same methodology and have found similar behaviour at a qualitative level. Of course, the results will depend on the particular details of the parametrization schemes employed in a given model and the ways in which these schemes interact with each other. However, a split between parametrized convection and large-scale latent heating is present in all numerical models for which the grid length is not convection permitting. Due to the high precipitation efficiency of the WCB, the total precipitation associated with an extratropical cyclone will mainly be determined by the moisture supply into the WCB (cf. Done *et al.*, 2006; Boutle *et al.*, 2011). However, the balance between parametrized convection and large-scale latent heating will depend on the tunings and formulations of the two parametrizations.

We have shown that changing the strength of the convection parametrization scheme has an effect on the model's response in terms of

  (i) the convective–large-scale partition of precipitation, and
  (ii) the transport of air masses through the WCB in a simulation of an extratropical cyclone.

As such, this study presents a framework to study systematically the effects of the convection parametrization tuning on these two aspects of the model's response. This systematic study would require a measure of these effects, for which the spatially integrated rain rates might prove useful. Analyses using ensemble

simulations would also be beneficial in order to determine the robustness of the results. To investigate long-term effects, global simulations would be advisable in order to avoid boundary constraints on the development of the systems. However, this is material for future research.

Acknowledgements

References

Ahmadi-Givi F, Craig GC, Plant RS. 2004. The dynamics of a midlatitude cyclone with very strong latent heat release. *Q. J. R. Meteorol. Soc.* **130**: 295–323.

Arakawa A, Lamb V. 1977. Computational design of the basic dynamical processes of the UCLA General Circulation Model. *Methods Comput. Phys.* **17**: 173–265.

Bechtold P, Köhle M, Jung T, Doblas-Reyes F, Leutbecher M, Rodwell MJ, Vitart F, Balsamo G. 2008. Advances in simulating atmospheric variability with the ECMWF model: From synoptic to decadal time-scales. *Q. J. R. Meteorol. Soc.* **134**: 1337–1351.

Boutle IA, Belcher SE, Plant RS. 2011. Moisture transport in midlatitude cyclones. *Q. J. R. Meteorol. Soc.* **137**: 360–373.

Browning KA. 1990. Organisation of clouds and precipitation in extratropical cyclones. In *Extratropical Cyclones: The Erik Palmén Memorial Volume*, Newton C, Holopainen EO (eds). 129–154. American Meteorological Society: Boston, MA.

Carlson TN. 1980. Airflow through midlatitude cyclones and the comma cloud pattern. *Mon. Weather Rev.* **108**: 1498–1509.

Chagnon JM, Gray SL, Methven J. 2013. Diabatic processes modifying potential vorticity in a North Atlantic cyclone. *Q. J. R. Meteorol. Soc.* **139**: 1270–1282.

Charney JG, Phillips NA. 1953. Numerical integration of the quasi-geostrophic equations for barotropic and simple baroclinic flows. *J. Meteorol.* **10**: 71–99.

Davies T, Cullen MJP, Malcolm AJ, Mawson MH, Staniforth A, White AA, Wood N. 2005. A new dynamical core for the Met Office's global and regional modelling of the atmosphere. *Q. J. R. Meteorol. Soc.* **131**: 1759–1782.

Davis CA, Stoelinga MT, Kuo YH. 1993. The integrated effect of condensation in numerical simulations of extratropical cyclogenesis. *Mon. Weather Rev.* **121**: 2309–2330.

Didone M. 2006. 'Performance and error diagnosis of global and regional NWP models', PhD thesis, Swiss Federal Institute of Technology (ETH): Zurich, Switzerland.

Dirren S, Didone M, Davies HC. 2003. Diagnosis of 'forecast–analysis' differences of a weather prediction system. *Geophys. Res. Lett.* **30**: 2060, doi: 10.1029/2003GL017986.

Done JM, Craig GC, Gray SL, Clark PA, Gray MEB. 2006. Mesoscale simulations of organized convection: Importance of convective equilibrium. *Q. J. R. Meteorol. Soc.* **132**: 737–756.

Eckhardt S, Stohl A, Wernli H, James P, Forster C, Spichtinger N. 2004. A 15-year climatology of warm conveyor belts. *J. Clim.* **17**: 218–237.

Edwards J, Slingo A. 1996. Studies with a flexible new radiation code. Part I: Choosing a configuration for a large-scale model. *Q. J. R. Meteorol. Soc.* **122**: 689–719.

Fink AH, Pohle S, Pinto JG, Knippertz P. 2012. Diagnosing the influence of diabatic processes on the explosive deepening of extratropical cyclones. *Geophys. Res. Lett.* **39**: L07803, doi: 10.1029/2012GL051025.

Grams CM, Wernli H, Böttcher M, Campa J, Corsmeier U, Jones SC, Keller JH, Lenz CJ, Wiegand L. 2011. The key role of diabatic processes in modifying the upper-tropospheric wave guide: A North Atlantic case-study. *Q. J. R. Meteorol. Soc.* **137**: 2174–2193.

Grant ALM. 2001. Cloud-base fluxes in the cumulus-capped boundary layer. *Q. J. R. Meteorol. Soc.* **127**: 407–421.

Grant ALM, Brown AR. 1999. A similarity hypothesis for shallow-cumulus transports. *Q. J. R. Meteorol. Soc.* **125**: 1913–1936.

Gray SL. 2006. Mechanisms of midlatitude cross-tropopause transport using a potential vorticity budget approach. *J. Geophys. Res.* **111**: 14, doi: 10.1029/2005JD006259.

Gray SL, Martínez-Alvarado O, Baker LH, Clark PA. 2011. Conditional symmetric instability in sting jet storms. *Q. J. R. Meteorol. Soc.* **137**: 1482–1500.

Gregory D, Rowntree PR. 1990. A mass flux convection scheme with representation of cloud ensemble characteristics and stability-dependent closure. *Mon. Weather Rev.* **118**: 1483–1506.

Harrold TW. 1973. Mechanisms influencing distribution of precipitation within baroclinic disturbances. *Q. J. R. Meteorol. Soc.* **99**: 232–251.

Joos H, Wernli H. 2012. Influence of microphysical processes on the potential vorticity development in a warm conveyor belt: A case-study with the limited-area model COSMO. *Q. J. R. Meteorol. Soc.* **138**: 407–418.

Jung T, Miller MJ, Palmer TN, Towers P, Wedi N, Achuthavarier D, Adams JM, Altshuler EL, Cass BA, Kinter JL III, Marx L, Stan C, Hodges KI. 2012. High-resolution global climate simulations with the ECMWF model in Project Athena: Experimental design, model climate, and seasonal forecast skill. *J. Clim.* **25**: 3155–3172.

Lindstrom SS, Nordeng TE. 1992. Parameterised slantwise convection in a numerical model. *Mon. Weather Rev.* **120**: 742–756.

Lock AP, Brown AR, Bush MR, Martin GM, Smith RNB. 2000. A new boundary-layer mixing scheme. Part I: Scheme description and single-column model tests. *Mon. Weather Rev.* **128**: 3187–3199.

Martínez-Alvarado O, Joos H, Chagnon J, Boettcher M, Gray SL, Plant RS, Methven J, Wernli H. 2013. The dichotomous structure of the warm conveyor belt. *Q. J. R. Meteorol. Soc.* in press, doi: 10.1002/qj.2276.

Messori G, Czaja A. 2013. On the sporadic nature of meridional heat transport by transient eddies. *Q. J. R. Meteorol. Soc.* **139**: 999–1008.

Montgomery MT, Farrell BF. 1991. Moist surface frontogenesis associated with interior potential vorticity anomalies in a semi-geostrophic model. *J. Atmos. Sci.* **48**: 343–367.

Oort AH, Peixóto JP. 1983. Global angular momentum and energy balance requirements from observations. *Adv. Geophys.* **25**: 355–490.

Peixóto JP, Oort AH. 1984. Physics of climate. *Rev. Mod. Phys.* **56**: 365–429.

Pinto JG, Karremann MK, Born K, Della-Marta PM, Klawa M. 2012. Loss potential associated with European windstorms under future climate conditions. *Clim. Res.* **54**: 1–20.

Rauscher SA, Ringler TD, Skamarock WC, Mirin AR. 2013. Exploring a global multiresolution modeling approach using aquaplanet simulations. *J. Clim.* **26**: 2432–2452.

Sanders F, Gyakum JR. 1980. Synoptic-dynamic climatology of the 'bomb'. *Mon. Weather Rev.* **108**: 1589–1606.

Schäfler A, Dörnbrack A, Wernli H, Kiemle C, Pfahl S. 2011. Airborne lidar observations in the inflow region of a warm conveyor belt. *Q. J. R. Meteorol. Soc.* **137**: 1257–1272.

Schultz DM. 2001. Reexamining the cold conveyor belt. *Mon. Weather Rev.* **129**: 2205–2225.

Smith PJ. 1999. The importance of the horizontal distribution of heating during extratropical cyclone development. *Mon. Weather Rev.* **128**: 3692–3694.

Stoelinga MT. 1996. A potential vorticity-based study of the role of diabatic heating and friction in a numerically simulated baroclinic cyclone. *Mon. Weather Rev.* **124**: 849–874.

Tracton MS. 1973. The role of cumulus convection in the development of extratropical cyclones. *Mon. Weather Rev.* **101**: 573–593.

Trenberth KE, Stepaniak DP. 2003. Covariability of components of poleward atmospheric energy transports on seasonal and interannual timescales. *J. Clim.* **16**: 3691–3705.

Wernli H, Davies HC. 1997. A Lagrangian-based analysis of extratropical cyclones. I: The method and some applications. *Q. J. R. Meteorol. Soc.* **123**: 467–489.

Wernli H, Dirren S, Liniger MA, Zillig M. 2002. Dynamical aspects of the life cycle of the winter storm 'Lothar' (24–26 December 1999). *Q. J. R. Meteorol. Soc.* **130**: 405–429.

Whitaker JS, Davis CA. 1994. Cyclogenesis in a saturated environment. *J. Atmos. Sci.* **51**: 889–907.

Wilson DR, Ballard SP. 1999. A microphysically based precipitation scheme for the UK Meteorological Office Unified Model. *Q. J. R. Meteorol. Soc.* **125**: 1607–1636.

Yanai M, Esbensen S, Chu JH. 1973. Determination of bulk properties of tropical cloud clusters from large-scale heat and moisture budgets. *J. Atmos. Sci.* **30**: 611–627.

Zhu Y, Newell RE. 1994. Atmospheric rivers and bombs. *Geophys. Res. Lett.* **21**: 1999–2002, doi: 10.1029/94GL01710.